PHYSICS

Probing electron and hole colocalization by resonant four-wave mixing spectroscopy in the extreme ultraviolet

Horst Rottke[1]*, Robin Y. Engel[2,3], Daniel Schick[1], Jan O. Schunck[2,3], Piter S. Miedema[2], Martin C. Borchert[1], Marion Kuhlmann[2], Nagitha Ekanayake[2], Siarhei Dziarzhytski[2], Günter Brenner[2], Ulrich Eichmann[1], Clemens von Korff Schmising[1], Martin Beye[2,3], Stefan Eisebitt[1,4]*

Extending nonlinear spectroscopic techniques into the x-ray domain promises unique insight into photoexcited charge dynamics, which are of fundamental and applied interest. We report on the observation of a third-order nonlinear process in lithium fluoride (LiF) at a free-electron laser. Exploring the yield of four-wave mixing (FWM) in resonance with transitions to strongly localized core exciton states versus delocalized Bloch states, we find resonant FWM to be a sensitive probe for the degree of charge localization: Substantial sum- and difference-frequency generation is observed exclusively when in a one- or three-photon resonance with a LiF core exciton, with a dipole forbidden transition affecting details of the nonlinear response. Our reflective geometry–based approach to detect FWM signals enables the study of a wide variety of condensed matter sample systems, provides atomic selectivity via resonant transitions, and can be easily scaled to shorter wavelengths at free-electron x-ray lasers.

INTRODUCTION

Nonlinear wave mixing in the optical spectral range is a cornerstone of nonlinear optics. It has been used extensively for the generation of coherent light at otherwise inaccessible wavelengths, for the analysis of optical properties of materials, and, using ultrashort light pulses, to explore the evolution of optical excitations in time. Free-electron lasers (FELs) have opened the opportunity to apply these nonlinear techniques in the extreme ultraviolet (XUV) up to the x-ray spectral ranges. One promise of these approaches is that at sufficiently short wavelengths and pulse duration, electronic excitations may be followed on an atomic length and time scale. Moreover, XUV radiation makes it possible operate in resonance with core levels, providing element specificity and spectroscopic information with little lifetime broadening.

So far, however, there have been few studies on nonlinear processes in solids involving XUV or x-ray beams. Parametric down conversion, a second-order nonlinear process, aimed at probing valence-electron charge densities and the optical response of crystals with atomic resolution (*1*–*3*). With similar aims, second-order x-ray and optical sum-frequency mixing, essentially being optically modulated x-ray diffraction, has first been observed using FEL and long-wavelength optical laser radiation (*4*). Proof-of-principle experiments demonstrating second harmonic generation of x-rays in solids and interface sensitivity of second-order nonlinear processes in centrosymmetric crystals in the soft x-ray range have also been reported (*5*, *6*).

In contrast, four-wave mixing (FWM), as a third-order nonlinear process, is able to address the bulk properties of any material, irrespective of its symmetry. Here, first experimental investigations based on transient gratings induced by XUV FEL pulses and probed either by optical or even XUV laser pulses have been reported (*7*–*12*). Very recently, FWM in NaCl at the Na^+ $L_{2,3}$ edge near 33.5 eV, using laser-generated attosecond XUV and near-infrared (NIR) laser pulses, revealed the presence of dark excited states, i.e., states not dipole coupled to the electronic ground state of the material (*13*).

We report on the observation of a complementary FWM process driven in a solid, namely, sum- and difference-frequency generation (SFG and DFG, respectively) involving one XUV (ω_X) and two NIR photons (ω_I) with resulting beams at frequencies $\omega_{FWM} = \omega_X \pm 2\omega_I$, i.e., different from the radiation driving the process, which, to our knowledge, has not been observed yet. We study lithium fluoride (LiF), a prototypical ionic crystal with centrosymmetry. In particular, we investigate the effect of electronic excitations with a high degree of electron-hole correlation on these processes, using the presence of both strongly localized core excitons and delocalized Bloch states in LiF as a model to probe the degree of colocalization of the excited electron and hole.

Exploiting the wavelength tunability of the FEL source, we are able to chart the FWM conversion efficiency. We find significant SFG and DFG in LiF when in either one- or three-photon resonance with the core exciton that is linked with the Li^+ 1s2p excited electron configuration. An energetically near exciton, linked with the Li^+ 1s2s electron configuration and suspected to be present from linear absorption experiments, is seen—via comparison to theory—to affect the frequency conversion processes via two-photon resonance and a near-resonant one-NIR-photon coupling of both excitonic states. In contrast, we do not observe any FWM when exclusively in resonance with transitions to delocalized Bloch states in the experiment. This indicates that FWM in the XUV and soft x-ray spectral range is a sensitive probe of charge colocalization and charge separation. Given that the separation of holes and electrons and the localization of charge at particular atomic sites are key steps in (photo)chemical reactions, light harvesting, and the elementary steps of photovoltaics, we expect this sensitivity to be instrumental in the study of phenomena in materials science, physics, and chemistry in the future.

[1]Max-Born-Institut für Nichtlineare Optik und Kurzzeitspektroskopie, Max-Born-Straße 2A, 12489 Berlin, Germany. [2]Deutsches Elektronen-Synchrotron DESY, Notkestr. 85, 22607 Hamburg, Germany. [3]Department of Physics, Universität Hamburg, Luruper Chaussee 149, 22761 Hamburg, Germany. [4]Technische Universität Berlin, Institut für Optik und Atomare Physik, Straße des 17. Juni 135, 10623 Berlin, Germany.
*Corresponding author. Email: rottke@mbi-berlin.de (H.R.); eisebitt@mbi-berlin.de (S.E.)

RESULTS

The frequency mixing processes studied, one- and three-photon resonant with a LiF core exciton, are schematically illustrated in Fig. 1A. The core exciton of interest here is formed by the promotion of one of the strongly localized 1s core electrons of a Li^+ ion in LiF to an excited state equally localized on the same ion and linked with the Li^+ electronic configuration 1s2p. It gives rise to a dipole allowed transition with a characteristic narrow absorption structure in linear spectroscopy (*14*). We will refer to this final state as p-type exciton. The prominent, narrow resonance enhancement of the LiF reflectivity at 62.3-eV photon energy in Fig. 1B is attributable to this core exciton. The 1s2s excited electron configuration of the Li^+ ion is energetically close by but not dipole coupled to the $(1s)^2$ ground state configuration in a perfect cubic LiF crystal. We will refer to this 1s2s Li^+ electron configuration as s-type exciton. In linear absorption spectroscopy (*14*) and in the LiF linear reflectivity shown in Fig. 1B, a small low-energy shoulder of the p-type exciton feature, located at ≈61 eV, is suspected to be due to this s-type exciton, becoming weakly visible via dipole coupling to the $(1s)^2$ configuration through inversion symmetry breaking (*15*). In contrast, transitions into delocalized band states are responsible for the spectral features at higher photon energies in Fig. 1B (*16*–*19*).

We study FWM at the sum and difference frequencies $\omega_X \pm 2\omega_I$ by detecting the generated radiation emitted by a LiF single crystal toward the vacuum side, from where the process driving XUV and NIR laser beams are impinging. The scheme of the setup in Fig. 2 visualizes this detection approach; the experimental parameters are detailed in Materials and Methods. Note that an aluminum filter directly upstream of the detector not only blocks NIR radiation but also absorbs XUV with photon energies exceeding 72.7 eV.

In Fig. 3, we show our main experimental result, the dependence of the sum- and difference-frequency conversion yields on the setting of the FEL photon energy in a range covering the LiF core exciton and part of the conduction band. The density plot in Fig. 3A reveals the energy offset of the radiation generated by wave mixing with respect to the corresponding setting of the FEL photon energy. As directly evident from the experimental data, it amounts to $\pm 2\hbar\omega_I = \pm 3.1$ eV, i.e., two times the fixed NIR photon energy, for the generated sum and difference frequency with narrow spectral distributions. This spectral spacing is indicative of the wave mixing nature of the signals observed. Figure 3B presents individually the total number of sum- and difference-frequency photons generated in each FEL pulse train during XUV and NIR temporal overlap as a function of the photon energy of the process driving XUV radiation. On average, $(5.3 \pm 0.1) \times 10^{11}$ XUV photons per pulse train were impinging from the FEL on the LiF sample for the data shown in Fig. 3 (A and B). The direction of polarization of both, the FEL and NIR laser pulses, is in the common plane of incidence on the sample, and both pulses arrive simultaneously except for a statistically distributed relative arrival time jitter. The entire measurement is performed at a fixed NIR pulse intensity on the LiF crystal. As is obvious in Fig. 3 (A and B), we observe a significant yield of frequency conversion only when in resonance with the p-type core exciton located at $\hbar\omega_{exc} = 62.07$ eV. This can either be a one-photon resonance with the FEL photon energy tuned to resonance ($\omega_X \approx \omega_{exc}$) or a three-photon resonance satisfying $\omega_X \pm 2\omega_I \approx \omega_{exc}$. In both cases, SFG and

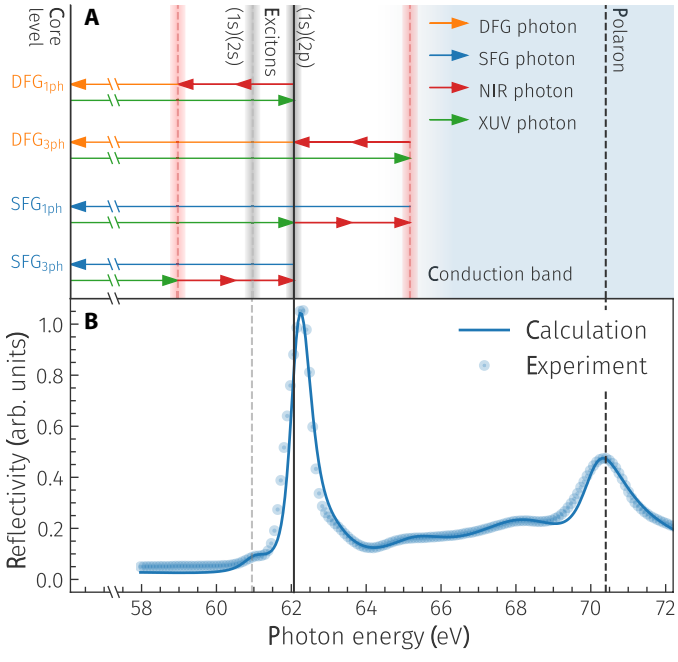

Fig. 1. FWM schemes and the LiF linear reflectivity. (**A**) Schematic view of the LiF level structure relevant to the experiment with the horizontal arrows representing SFG and DFG in one- and three-photon resonance with the p-type LiF core exciton at 62.07-eV photon energy, just below the conduction band edge. The green and red arrows depict the driving XUV and NIR photons, respectively. The blue and orange ones represent the generated sum- and difference-frequency photons, respectively. The shaded regions indicate the spectral bandwidth of the FEL. (**B**) The schematic level structure of (A) showing up in the linear reflectivity of LiF in the photon energy range relevant to the experiment. The blue dots represent the measured reflectivity. The line is the calculated reflectivity based on the model for the linear dielectric constant ϵ as outlined in the Supplementary Materials. The narrow reflectivity peak visible at 62.3 eV is due to the LiF p-type core exciton resonance located at 62.07 eV (vertical line) with one of the Li^+ $(1s)^2$ core electrons excited. Conduction band absorption is generally assumed to start at photon energies to the right of this resonance. arb. units, arbitrary units.

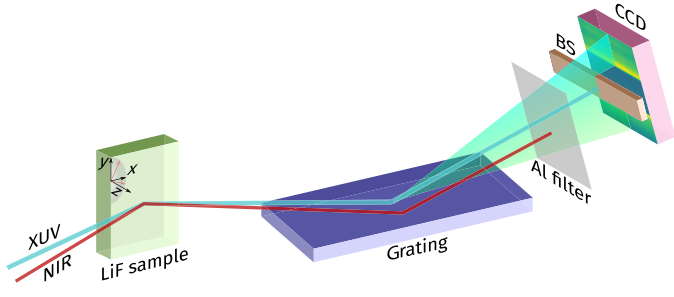

Fig. 2. Schematic view of the experimental setup. The FEL (blue), NIR (red), and the generated sum- and difference-frequency beams reflected off the LiF to vacuum interface are dispersed by a reflection grating. Subsequently, the NIR beam is blocked by an aluminum foil and the FEL beam by a separate beam stop (BS) directly in front of a charge-coupled device (CCD) camera that detects the generated sum- and difference-frequency beams. The XUV and NIR beams propagate in a common plane of incidence toward the LiF sample that we choose to be the *xz* plane of a suitably chosen Cartesian coordinate system with the *z* axis normal to the LiF surface and parallel to one of the LiF cubic crystal axes (see the axis system indicated on the LiF crystal surface). The two in-plane axes of the LiF crystal (red axes) were rotated by (22.5 ± 2.5)° with respect to the *x* and *y* axes of this coordinate system in the LiF surface plane.

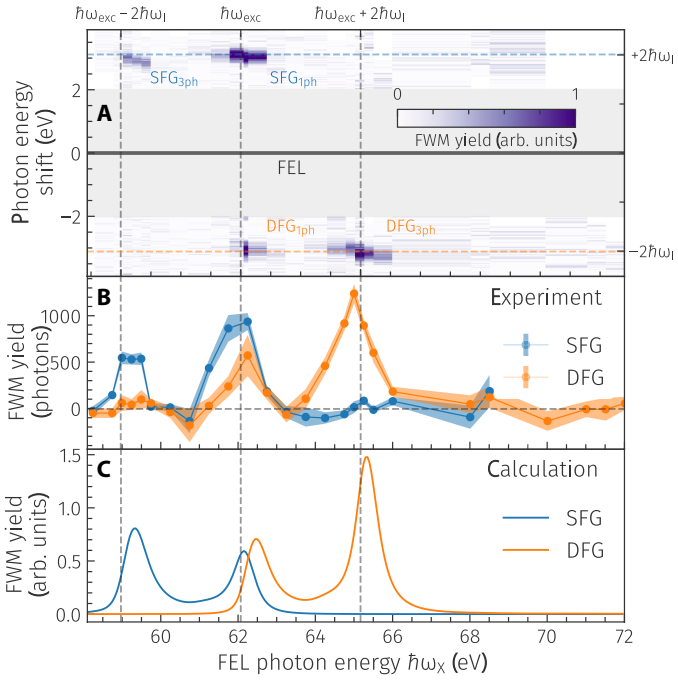

Fig. 3. Measured and calculated frequency conversion yields. (**A**) Density plot of the experimental spectral distributions of the generated sum- and difference-frequency photons (vertical axis) for the different FEL photon energy settings (horizontal axis). The spectral distributions are shown relative to the respective FEL photon energy settings. They thus appear at an offset of $\pm 2\hbar\omega_I = \pm 3.1$ eV with respect to the respective FEL photon energy (horizontal line at zero). (**B**) The generated number of sum- (blue) and difference-frequency (orange) photons plotted over the process driving FEL photon energy $\hbar\omega_X$. Shown is the total number of generated photons per FEL pulse train at zero FEL-NIR pulse delay summed over the whole spectral distribution of the generated radiation. Sizable frequency conversion is observed only with the incident FEL and NIR radiation in one- or three-photon resonance with the p-type core exciton of LiF. (**C**) Calculated sum- and difference-frequency yields plotted as functions of the process driving FEL photon energy. The NIR photon energy is fixed at 1.55 eV. The plot is based on our basic model of the LiF third-order nonlinear susceptibility tensor in this photon energy range and corresponds to the parameter $R = 0.112$ in Fig. 5. Shaded areas in (B) connect 95% confidence intervals of the data.

DFG are observed as sketched in Fig. 1A. Aside from these settings, no FWM frequency conversion was detectable above the residual background level of FEL stray light.

Further corroboration of the FWM nature of the signals shown in Fig. 3 comes from a detailed analysis of (i) the direction of propagation and divergence of the individual beams observed and (ii) their spectral and (iii) temporal behavior. Details of these characteristics of the generated radiation beams are shown in Fig. 4, exemplified for DFG in three-photon resonance with the LiF p-type core exciton, obeying ($\omega_X - 2\omega_I = \omega_{exc}$).

Regarding (i): We treat an FWM process, where the driving radiation impinges (Fig. 2) from the vacuum side. In this case, the emission direction of sum- and difference-frequency beams emitted by the medium toward the vacuum side is fixed through boundary conditions given by the driving FEL and NIR fields at the crystal interface to vacuum, via the induced nonlinear polarization in the medium. Fundamentally, this amounts to momentum conservation at the vacuum-medium interface, with the components of the driving fields' wave vectors along the interface on the vacuum side being the relevant quantities. In the experiment, the angle enclosed between the FEL and NIR beams is rather small ($|\theta_X - \theta_I| = 0.75^\circ$), resulting in a practically collinear geometry, and moreover, $\omega_X \gg \omega_I$. Therefore, the nonlinear reflection is expected closely along the reflected FEL beam with an estimated offset angle α of $|\alpha| < 0.04^\circ$ (see the Supplementary Materials for more details). This angle is much smaller than the radial divergence of the FEL beam, which can be determined to be 0.12° using the characteristics of the focusing x-ray optics. The beam directions observed are thus in line with momentum conservation and the presence of an FWM process in our geometry. This shows that the generated signal keeps the typical directional characteristics of an FWM signal in contrast to, e.g., a fluorescence emission channel. To discriminate the beams, the experimental geometry requires a spectral separation of the FEL beam and the nonlinear reflection rather than a spatial separation (see Fig. 2). An example for a difference-frequency beam profile on the charge-coupled device (CCD) camera as projected on the direction perpendicular to the dispersion direction of the grating is shown in Fig. 4A. The full width of this beam amounts to ≈4 mm at half maximum (FWHM), corresponding to a far-field radial beam divergence of ≈0.09°. As expected, the nonlinear emission cone is limited by the divergence of the focused XUV and NIR laser beams that drive the nonlinear processes.

Regarding (ii): In Fig. 4D, we show the spectral distribution of the frequency conversion yield over the relative delay of the FEL and NIR pulses. A cut through this density plot along a line at zero delay, i.e., the detailed spectral distribution of the $\omega_X - 2\omega_I$ difference-frequency photon yield, is displayed in Fig. 4B. The distribution is centered at 62.05 eV, which is in close agreement with the expectation according to energy conservation requiring $\hbar\omega = \hbar\omega_X - 2\hbar\omega_I = 62.15$ eV. The bandwidth of the FEL varies between 500 and 600 meV FWHM, depending on photon energy, while the bandwidth of the NIR pulses is close to 100 meV. Thus, observing the bandwidth of the SFG and DFG signals with an FWHM of 351 meV suggests that the wave mixing process is limited by the natural linewidth of the excitonic lithium *K*-edge resonance.

Regarding (iii): The dependence of the difference-frequency yield on the time delay between the FEL and NIR pulses in Fig. 4C indicates that the nonlinear conversion process requires temporal overlap of the pulses. This is expected for a nonlinear wave mixing process for which the induced nonlinear polarization decays on a time scale faster than the widths of the driving laser pulses. The observed temporal profile represents the cross-correlation of the FEL and NIR pulses including the relative timing jitter of the pulses on the LiF sample. A Gaussian fit to the yield indicates an FWHM of this cross-correlation of the pulses of (180 ± 22) fs. Because the NIR laser pulse width was 21 fs and the FEL pulse width was set to be less than 100 fs, a substantial contribution of ≈140 fs to the width of the cross-correlation curve is actually due to the relative arrival time jitter of the pulses on the LiF sample.

DISCUSSION

Having firmly established that the signals that we observe are due to FWM, we now turn our attention to the pronounced variation of the photon yield of the $\omega_X \pm 2\omega_I$ wave mixing processes as a function of the driving FEL photon energy seen in Fig. 3B. How does the nature of the resonances involved influence this yield? Obviously, significant frequency conversion is present only in close one- or three-photon

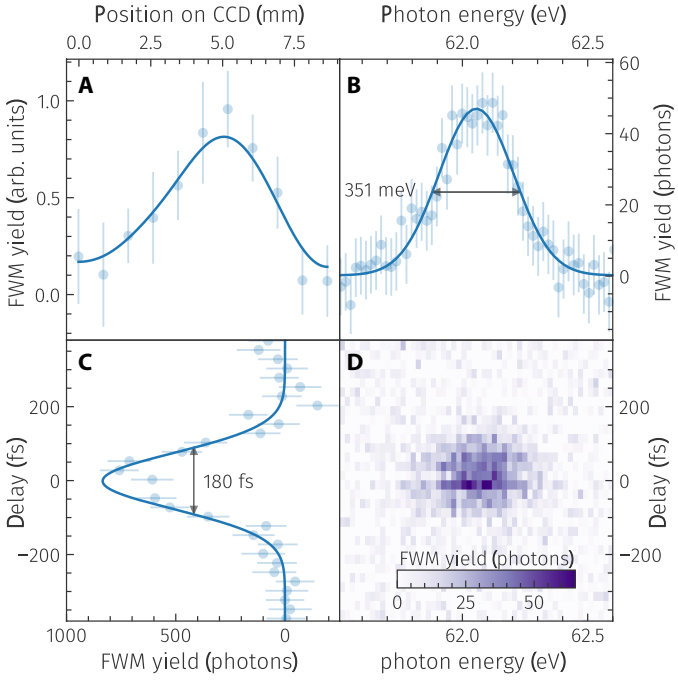

Fig. 4. Characteristic details of the radiation generated in the nonlinear processes. As a characteristic example, we present details for the difference-frequency beam with the FEL tuned to three-photon resonance with the LiF core exciton at $\hbar\omega_X = 65.25$ eV. (**A**) Sample profile of the generated difference-frequency beam on the CCD camera perpendicular to the dispersion direction of the grating. The blue curve is intended to guide the eye. (**B**) Spectral distribution of the difference-frequency photon yield with the FEL-NIR pulse delay set to zero, i.e., a cut through the density plot in (**D**) along a line at zero delay. (**C**) The total amount of generated difference-frequency photons plotted over the FEL-NIR pulse delay, i.e., a projection of the density plot in (D) on the delay axis. Blue curves in (B) and (C) represent Gaussian fits to the data, and arrows indicate their FWHM. Error bars represent the SD. The maximum of the Gaussian fit in (C) is shown in Fig. 3B as the DFG yield at $\hbar\omega_X = 65.25$ eV. (D) Density plot of the dependence of the spectral distribution of the difference-frequency photon yield on the FEL-NIR pulse delay.

resonance with the p-type core exciton, giving rise to the characteristic two-peak structure in both the $\omega_X + 2\omega_I$ and $\omega_X - 2\omega_I$ photon yields, separated by approximately $2\omega_I$ in Fig. 3B. In contrast, one- or three-photon resonance exclusively with conduction band states does not give rise to detectable frequency conversion, i.e., no FWM yield was observed with an FEL photon energy setting higher than ≈64 and ≈67 eV for sum- and difference-frequency mixing, respectively.

The influence of electronic correlation and, in particular, the formation of a core exciton next to the Li^+ *K*-edge absorption have been studied in the past (*14*), and first-principles calculations indicate that strong correlation effects between the core hole and the electrons are restricted to the first few electron volts of the XUV absorption starting at ≈60 eV (*20*). The nature of the electronic states involved in linear absorption and correspondingly in the linear reflectivity of LiF in Fig. 1B can explain what we observe in FWM. In the initial state, the active electron is well localized on a Li atom in the crystal. This also is true for the p-type core exciton, where the excited electron remains localized in the vicinity of that same Li atom (*15*). The corresponding overlap of the wave function with other localized states of the lithium atom enhances the respective transition matrix elements, i.e., the probability that a suitable photon may drive a transition between colocalized states. In other words, a colocalization of excited states strongly enhances the third-order nonlinear susceptibility $\chi^{(3)}$ of LiF, which is the quantity responsible for the FWM processes that we study. In contrast, the higher-energy conduction band electronic states can be described by delocalized Bloch states with the excited electron being able to move freely in the crystal. The lack of colocalization in this case can, in turn, give rise to a strongly suppressed $\chi^{(3)}$. This difference in electron-hole colocalization is reflected in the observed frequency conversion yield in Fig. 3B.

Specifically, we note that we observe no significant DFG when tuning the FEL photon energy to the 70.5-eV feature in the linear reflectivity spectrum Fig. 1B. The corresponding feature in the LiF near *K*-edge absorption fine-structure spectrum has been debated to be due to correlation effects, namely, an electron polaron (*21*, *22*). Furthermore, it has been speculated that this electron polaron is bound to the Li 1s core hole (*21*). While this debate is about half a century old, ab initio electronic structure calculations, to this day, have not been able to address this question. Our experiment can address this question experimentally: In the hypothesized case of a bound polaron, an increase of the nonlinear susceptibility and hence the FWM yield would be expected in one- and three-photon resonance with the 70.5-eV feature. However, no significant FWM yield was observed either in the three-photon resonant sum-frequency yield (Fig. 3B, blue curve around 67.4 eV) nor in the one-photon resonant difference-frequency yield (Fig. 3B, orange curve around 70.5 eV). This indicates the absence of colocalization of the active electron and core hole of the same order of magnitude as it is present for the core p-type exciton at 62.07 eV.

Next, we strive to obtain a basic understanding of the pronounced sum- and difference-frequency conversion yield when in resonance with the p-type core exciton. Given the strong localization and hence roughly atomic character of the core exciton, we model the third-order nonlinear susceptibility tensor $\chi^{(3)}$, which is not known for LiF in the relevant photon energy range, by involving Li^+ ionic states, namely, the $(1s)^2$ ground state and excited states corresponding to the p-type and to the s-type exciton. This approach is in analogy to the early efforts to understand the linear absorption spectrum (*23*). The details of the model are presented in Materials and Methods and in the Supplementary Materials.

On the basis of this $\chi^{(3)}$ model in conjunction with the experimental parameters, we obtain the conversion yields for the generated reflected sum- and difference-frequency beams as functions of the driving FEL photon energy as shown in Fig. 5. It is assumed that the polarization of both the FEL and NIR radiation is in their common plane of incidence on the LiF crystal and their angle of incidence is 52° with respect to the crystal normal as it was in the experiment. In Fig. 5B, we present the dependence of the difference-frequency yield on the applied FEL photon energy. Here, the ratio R of the radial parts of the Li^+ dipole matrix elements for the (1s2s) − (1s2p) (d_2) and $(1s)^2$ − (1s2p) (d_1) transitions $R = d_2/d_1$ serves as a parameter to characterize the relative influence of the states on $\chi^{(3)}$ and thus on the nonlinear polarization of the medium. The electric field strengths of the incident XUV and NIR radiation are assumed as constant. In Fig. 5A, we show the corresponding results for SFG.

At $R = 0$, the LiF s-type core exciton does not influence the frequency conversion at all. The resonance structure found thus exclusively originates from the driving laser radiation being either

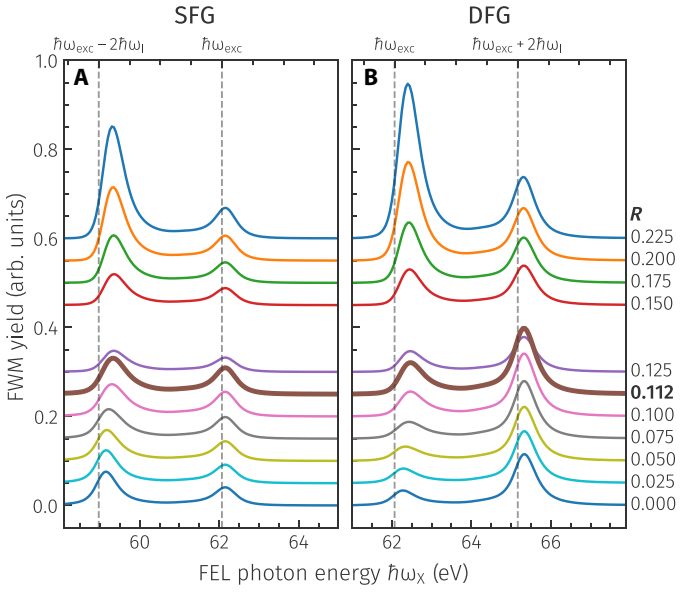

Fig. 5. Calculated frequency conversion efficiencies. Sum- (**A**) and difference-frequency mixing (**B**) yields calculated for the beams emitted from the LiF sample toward the vacuum side (reflection geometry; see Fig. 2). Shown are the dependencies of the efficiencies on the photon energy $\hbar\omega_X$ of the incident FEL radiation when scanned over the LiF p-type core exciton at $\hbar\omega_{exc} = 62.07$ eV for a set of values of the parameter R starting at zero up to $R = 0.225$. R quantifies the dipole coupling strength of the LiF p-type to the s-type core exciton, the latter being separated in energy from the former by 1.1 eV, i.e., somewhat less than one NIR photon energy $\hbar\omega_I = 1.55$ eV. For comparison purposes, the conversion efficiency scales in (A) and (B) are chosen to be identical. Compared to the lower group of curves, the calculated efficiencies for the upper group have been scaled by a factor of 0.5. In both panels, we highlighted the efficiency curves for $R = 0.112$, which most closely reproduce the conversion yield structures found in the experiment (thick brown lines; see also Fig. 3C).

in one-photon ($\omega_X \approx \omega_{exc}$) or three-photon ($\omega_X \pm 2\omega_I \approx \omega_{exc}$) resonance with the p-type core exciton. The slight offset of the frequency conversion maxima toward a higher FEL photon energy as compared with the p-type exciton position ($\omega_{exc} = 62.07$ eV, table S1 and indicated by vertical lines in Fig. 5) can be attributed to the strong variation of the linear dielectric constant over the p-type exciton (fig. S2) accompanied by strong absorption of either the driving or generated radiation on resonance. For DFG, a shifting of the conversion maximum at $\omega_X \approx \omega_{exc}$ toward a higher FEL photon energy is predicted with increasing R (Fig. 5B), whereas the maximum at $\omega_X \approx \omega_{exc} + 2\omega_I$ does not shift. Moreover, the conversion efficiency peak at $\omega_X \approx \omega_{exc}$ gains strongly in amplitude with rising R. The underlying reason is a rising contribution of two-photon resonance with the s-type exciton relative to one–XUV photon resonance ($\omega_X \approx \omega_{exc}$) with the p-type exciton. Two-photon resonance with the s-type exciton would occur at $\omega_X = 62.52$ eV, compared to one–XUV photon resonance with the p-type exciton at $\omega_X = 62.07$ eV. A rising value of R represents a stronger coupling between s- and p-type core excitations. Thus, the rising conversion efficiency and shift are a consequence of the s-type exciton providing an intermediate two-photon resonance in the three-photon DFG process, as the 1.55-eV NIR photons are not far off resonance with the energy difference of 1.1 eV between s- and p-type excitons. In contrast, at three-photon resonance with the p-type exciton ($\omega_X \approx \omega_{exc} + 2\omega_I$), the frequency difference $\omega_X - \omega_I$ is well off the two-photon resonance with the s-type exciton. This results in a negligible effect of two-photon resonance on the corresponding difference-frequency conversion yield and on the position of the yield maximum.

A similar interpretation holds for the changes observable in the sum-frequency conversion yield with rising values of the parameter R in Fig. 5A. However, in this case, the conversion yield maximum at $\omega_X \approx \omega_{exc} - 2\omega_I$, originating from three-photon resonance with the p-type exciton, is affected by two-photon resonance with the s-type exciton, whereas the $\omega_X \approx \omega_{exc}$ conversion maximum, representing one–XUV photon resonance with the p-type exciton, is not. Combined, the model particularly predicts the difference-frequency conversion yield maximum at $\omega_X \approx \omega_{exc}$ appearing at a slightly higher FEL photon energy than the corresponding sum-frequency yield maximum and links it to the NIR photons being able to cause a coupling between s- and p-type excitons for $R > 0$.

Comparing the outcome of our model (Fig. 5) with the resonance structure observed in the experiment leads to an estimated R of approximately 0.112 when basing the comparison on the relative strengths of the frequency conversion yield maxima. For the purpose of direct comparison with the experiment, we show this calculated result in Fig. 3C for both SFG and DFG. To illustrate the precision of this estimate, a transition moment ratio of $R = 0.225$ changes the resonance behavior of the frequency conversion processes completely in a way that is significantly different from the experimental result. Similarly, $R = 0$ is not compatible with the experiment. In the model, $R \approx 0.112$ already results in a clear offset of the calculated difference-frequency conversion yield maximum at $\omega_X \approx \omega_{exc}$ to a higher FEL photon energy as compared to the corresponding sum-frequency yield maximum (Fig. 3C). A hint at such a shift can also be found in the experimental data in Fig. 3B at $\omega_X \approx \omega_{exc} \approx 62$ eV.

Within the limitations of our simple $\chi^{(3)}$ model, we are able to understand the experimental observations quantitatively, particularly the energy positions and relative yields of the FWM processes in LiF when in resonance with Li^+ 1s core excitations, including the significance of a dipole coupling of the p-type to the s-type exciton in the nonlinear response. The model calculation reproduces the significant sum- and difference-frequency conversion yield when close to one- and three-photon resonance with the p-type core exciton. While being in resonance with the p-type exciton is key for efficient frequency mixing, a two-photon resonance with the s-type exciton does affect the frequency conversion because a close to one-photon resonant, dipole allowed, coupling of the s- and p-type core excitons is present, mediated by the NIR laser pulses. Thus, our findings further corroborate the assignment of the low-energy shoulder of the linear reflection maximum observable at 61 eV in Fig. 1B due to an s-type exciton (*15*, *18*).

For NaCl, the observation of a complementary FWM process has recently been reported in a purely laser-based experiment, involving excitons related to the excited Na^+ 3s state with a hole in its closed 2p shell (*13*). This experiment revealed the presence of dark excited states that appear only in nonlinear spectroscopy besides bright excitonic excitations observable in linear absorption. A potential coherent lifetime of the nonlinear polarization induced in LiF as it was reported for NaCl on a time scale of 10 fs in (*13*) is too short to be detectable with our present temporal resolution. With recent advances of pushing x-ray–optical relative pulse jitter at FELs to below 25 fs (*24*) and the availability of both x-ray and

optical pulses in the few femtoseconds or even attosecond domain (*25*, *26*), we expect that such information for processes involving core excitations may also become accessible by our FEL-based approach and extendable to suitable resonances in the multi–kilo–electron volt photon energy range.

From an experimental point of view, we note that the third-order nonlinear process studied in this work, i.e., SFG and DFG, allows for easy spectroscopic discrimination of the nonlinear signal from the incident XUV or x-ray radiation, which is particularly important when mixing harder x-rays with laser pulses in the optical spectral range due to the challenge posed by an increasingly small angular separation. Furthermore, we note that the observation of a nonlinear process in reflection from a solid sample–vacuum interface is convenient in particular in the XUV spectral range (*27*, *28*), because, due to strong absorption, only very thin samples can typically be used to detect the generated radiation propagating through the nonlinear medium, e.g., a sample of 50-nm thickness was used in (*13*). We expect both these aspects as demonstrated here to be of relevance for the application of nonlinear x-ray spectroscopy in materials science, where tailoring the samples under study to experiments is only viable to a limited extent. Nevertheless, detecting transmitted radiation may be advantageous in selected cases where phase matching ($k_z - \tilde{k}_z = 0$ in eq. S11) can be exploited, provided that the propagation lengths of the FEL and optical and generated radiation in the sample can be made long enough before efficient absorption limiting the detectable signal. At interfaces of centrosymmetric crystals to vacuum or to other materials, a loss of inversion symmetry is commonly used to obtain surface or interface sensitivity via observation of second harmonic generation in the optical regime. As we have demonstrated, third-order nonlinear signals can now be detected in one- and three-photon resonance with specific inner shell excitations. Looking ahead, the combination of second- and third-order nonlinear frequency conversion involving x-rays will allow one to differentiate between bulk- and surface-specific contributions to the nonlinear polarization of a material.

Our work demonstrates that FWM under resonant conditions is a sensitive probe of charge localization, allowing for atomic specificity even when using wavelengths substantially larger than the unit cell of the system of interest. While scalable to hard x-rays, we note that even when carried out with soft x-rays, our approach can complement the atomic scale information on the valence charge distribution obtainable with wavelengths comparable to the interatomic spacing (*4*) and mesoscale information with a length scale defined by a transient grating period (*7*–*9*). Nonlinear spectroscopy with few-femtosecond x-rays gives access to otherwise forbidden, dark transitions and hence information beyond the linear spectroscopy dominating current x-ray spectroscopy. We note that our approach of exploiting core-hole resonances differs from some studies based on nonresonant hard x-ray wave mixing (*29*–*31*): The nonresonant methods can be understood as a wave mixing probe, which is scattering from an electronic system that was modified by one or more optical pump pulses. In contrast, our approach probes the coupling between core-excited states following an x-ray pump. As core holes are generally strongly localized, we gain selective spectroscopic information on optically "dark" states local to targeted sites in the probed system. We did not observe nonresonant wave mixing because LiF in its ground state is transparent for the 1.55-eV NIR pulses due to its large bandgap. The charge density remained mostly unperturbed by the optical laser alone. With the dynamics of transient localization and delocalization of charge at different atomic species being of fundamental importance for a multitude of processes not only in physics, chemistry, and biology but also in materials design, e.g., for light harvesting applications, we expect wave mixing processes in resonance with inner shell excitations to become a particularly fruitful approach for future time domain studies at FELs.

MATERIALS AND METHODS

Experiment

The experiment was carried out on the beamline FL24 of the FLASH2 FEL using the MUSIX (multidimensional spectroscopy and inelastic x-ray scattering) end station (*32*). A schematic view of the setup is shown in Fig. 2. The FEL delivered pulses in bunch trains with 40 laser pulses per train at a train repetition rate of 10 Hz. The pulse separation within each train was 10 μs, i.e., a pulse repetition rate of 100 kHz. The FEL beam was attenuated using a gas attenuator filled with 1.1×10^{-2} mbar of neon and a silicon attenuator foil of 411-nm thickness. The beam path was constrained by five beam diameters limiting irises: the first three with a diameter of 7.5 mm, and the latter two with a diameter of 10.0 and 10.5 mm, respectively. A focusing Kirkpatrick-Baez active optics system (KAOS) was used to focus the beam on the LiF sample (*33*). The spot size on the LiF crystal is estimated to be 150 μm FWHM in diameter as gauged with an yttrium aluminum garnet (YAG) scintillation screen. While the duration of the FEL pulses was not measured during the experiment, it was tuned to be less than 100 fs. The spectral bandwidth of the FEL pulses was determined from the measurements used for spectrometer calibration and varied between 0.5 and 0.6 eV, depending on photon energy. The angle of incidence of the beam on the LiF sample with respect to its surface normal was 52°. The energy of individual FEL pulses on the sample was (130 ± 25) nJ. This energy and the corresponding number of photons impinging on the LiF sample per pulse were determined by using an x-ray gas monitor detector upstream of the FEL beam and multiplying these data by an estimated beamline transmission up to the sample (*34*). The Supplementary Materials provides further details on the transmission estimates of the beamline.

The optical laser system was based on optical parametric chirped pulse amplification (OPCPA) synchronized to the FEL pulses and operated at a fixed photon energy of 1.55 eV. It delivered pulse trains identical in structure to those of the FEL with pulses of 21 fs in width (FWHM). The NIR laser beam was focused on the LiF sample using a lens pair with −250- and 750-mm focal lengths, respectively. After passing through a λ/2-wave plate and polarizer for adjusting the pulse energy and a second half-wave plate for turning its polarization, the linearly polarized NIR beam was aligned nearly collinear with the FEL beam path by reflecting it off a flat 90° silver-coated turning mirror that passed the FEL beam through a center hole (5-mm diameter). Thereby, the NIR laser beam enclosed a small angle of (0.75 ± 0.03)° with the FEL beam, propagating in the plane of incidence spanned by the FEL beam and the LiF surface normal, which coincided with one of the LiF crystal axes. This plane of incidence is assumed to be spanned by the x and z axes of a suitably chosen coordinate system as shown in Fig. 2. The two LiF crystal axes in the interface plane to vacuum, i.e., the two red axes in Fig. 2, enclosed an angle of (22.5 ± 2.5)° with the x and y axes of this coordinate system, respectively. The polarization vectors of the FEL and NIR pulses were located in the plane of incidence. The NIR

laser pulse energy on the LiF target was (68.0 ± 1.5) μJ with the spots of the FEL and NIR beams spatially overlapping.

The LiF sample was a single, (100) cut crystal with the crystal surface polished. With a thickness of 3 mm, it was transparent to the NIR laser beam, whereas the FEL beam was practically absorbed within ≈100 nm into the crystal, thus limiting the SFG and DFG to a narrow stretch below the crystal surface. The NIR, FEL, and generated sum- and difference-frequency beams reflected off the LiF sample were dispersed by a reflection grating and directed to a CCD camera positioned behind an aluminum filter (200-nm thickness), which not only blocked the NIR beam and stray light but also inhibited the detection of FWM signals beyond the aluminum *K*-edge at 72.7 eV. The specular reflection of the FEL beam was blocked by a narrow beam stop placed directly in front of the CCD camera (see Fig. 2).

The dispersion grating with spherical shape and varied line spacing was used to separate the FEL radiation from the generated sum- and difference-frequency radiation (*32*). It was operated at grazing incidence (2.1° grazing angle) and imaged the radiation spectrum onto the CCD camera. Because of the large radius of curvature of the grating (≈13.9 m), it had little influence on the divergence of the sum- and difference-frequency beams on their way from the LiF sample to the camera along the direction orthogonal to the dispersion direction of the grating. The length of the spectrometer setup, i.e., the separation of the LiF sample from the camera via the grating, was 1.33 m.

The back-illuminated CCD camera (Greateyes model GE-VAC 2048 2048) used to detect the XUV radiation was mounted in the vacuum chamber (*32*). Its detector consisted of 2048 by 2048 square pixels of 13.5 μm in size (*32*). For the experiment, 4 detector pixels were binned along the direction of dispersion of the spectrometer grating and 64 along the orthogonal direction to optimize the camera sensitivity. To speed up the readout rate, only 11 binned pixels perpendicular to the dispersion direction of the grating were read out. Thus, each stored camera image consisted of 512 × 11 image points. The detector accumulated the light of individual pulse trains, i.e., of 40 laser pulses before being read out. Limited by the detector readout speed, a frame rate of 5 Hz was achieved, meaning that the sum- and difference-frequency light generated by every second FEL pulse train was captured.

In the experimental runs, the FEL photon energy was tuned in steps in the range between approximately 58 and 72 eV. The FWM yields shown in Fig. 3 (A and B) were measured over the course of about 100 hours with individual datasets recorded for about 30 to 60 min on each single spot on the LiF sample at each FEL photon energy setting as a precaution against potential sample damage. We did, however, not observe systematic changes to the FWM yield measured in the first and last minutes of measurement on a given spot. At each energy setting, the delay between the XUV and NIR pulses was scanned within a 1- to 2-ps interval around the time overlap. This allowed to account for slow drifting of the XUV pulses' arrival time relative to that of the NIR pulses, which would have affected the FWM efficiency. The CCD camera recorded the radiation generated by FWM spectrally dispersed by the spectrometer grating. The recorded spectra were scaled to estimate the absolute number of photons actually generated by FWM in the LiF sample (see the Supplementary Materials for details). Fluctuations in optical stray light, generating a varying offset to each spectrum, were compensated by subtracting the average signal recorded in the FEL beam block shadow from each spectrum. Intensity fluctuations in the FEL beam were mitigated by normalizing the spectra such that the FEL stray light level of each spectrum equals the ensemble average. From these spectral distributions, a mean stray light spectrum was determined by averaging overall spectra recorded at FEL-NIR pulse delays larger than ±250 fs, leaving only the FWM signal together with a small, however fluctuating, residual background level. These spectra were then sorted by the XUV-NIR delay into delay-time bins of 25 fs with an average FWM spectrum computed for each bin. The result is a two-dimensional map of the FWM signal over the XUV-NIR delay and the energy distribution of the spectrally dispersed generated photons, as shown in Fig. 4D. While the average spectrum was calculated by the simple mean for each photon energy, an estimate of the uncertainty of this mean was computed as the SD of the averaged photon yields divided by the square root of the number of spectra in the respective bin, resulting in spectra such as shown in Fig. 4B for each delay bin. To derive the FWM yield shown in Fig. 3B, these delay-dependent spectra were integrated within ±500 meV of the expected photon energy of the FWM signal to form a delay trace as shown in Fig. 4C, which was then fitted by a Gaussian using the Levenberg-Marquardt algorithm. This fit was weighed with the inverse square uncertainty of the spectra. The maximum of this Gaussian represents the FWM yield at time overlap that is depicted in Fig. 3B. The error bars are derived from the fit and represent the SD of the fit result. Conversely, the FWM yield shown as a spectrally resolved colormap in Fig. 3A is an integration of FWM yields measured within ±250 fs of the expected time overlap.

The linear reflection of LiF shown in Fig. 1B was measured separately at the PM3 beamline of the BESSY II facility (*35*) using tunable synchrotron radiation linearly polarized in the plane of incidence of the beam. The angle of incidence on the LiF single crystal was 50° with respect to the surface normal of the sample.

Theoretical modeling of third-order FWM

The nonlinear reflection off a medium with a plane boundary to vacuum in the *xy* plane of a suitably chosen coordinate system (see Fig. 2) is connected with the generated electric field on the vacuum side. In the monochromatic, plane wave limit, this electric field can be represented by

$$\mathbf{E}_r = \mathbf{A}_r \exp\left(i\mathbf{k}_r\mathbf{x} - i\omega t\right) \tag{1}$$

where $\mathbf{A}_r$ is the amplitude and $\mathbf{k}_r = (k_x, 0, k_{rz})$ is the wave vector on the vacuum side ($k_{rz} > 0$) satisfying the dispersion relation $\mathbf{k}_r^2 = k_x^2 + k_{rz}^2 = (\omega/c)^2$ (c, the speed of light). The amplitude $\mathbf{A}_r$ can be found to be (for the derivation, see the Supplementary Materials)

$$\boldsymbol{A}_r = \frac{4\pi}{\tilde{k}_z + k_z}\left(\frac{(\tilde{k}_z P_x + k_x P_z)}{\tilde{k}_z - \epsilon k_{rz}}\begin{bmatrix} k_{rz} \\ 0 \\ -k_x \end{bmatrix} - \left(\frac{\omega}{c}\right)^2 \frac{P_y}{\tilde{k}_z - k_{rz}}\begin{bmatrix} 0 \\ 1 \\ 0 \end{bmatrix}\right) \tag{2}$$

This expression presumes a monochromatic, plane nonlinear polarization wave $\mathbf{P}\exp(i\mathbf{kx} - i\omega t)$ propagating into the medium that is assumed to be located in the half-space $z < 0$ with frequency ω and wave vector $\mathbf{k} = (k_x, 0, k_z)$ chosen to be located in the *xz* plane (see Fig. 2). The real and the imaginary parts of k_z are negative numbers, representing propagation of the nonlinear polarization into the medium

and absorption of the fields driving it. $\tilde{\mathbf{k}} = (k_x, 0, \tilde{k}_z)$ in Eq. 2 is the wave vector of the generated electric field at frequency ω propagating in the nonlinear medium. It satisfies the dispersion relation $\tilde{\mathbf{k}}^2 = k_x^2 + \tilde{k}_z^2 = (\omega/c)^2 \epsilon(\omega)$, where $\epsilon(\omega)$ is the dielectric constant of the medium at the frequency ω of the generated field. In the medium, it propagates with the nonlinear polarization and experiences linear absorption, meaning that the real and the imaginary parts of $\tilde{k}_z$ are negative numbers. k_x—the wave number component in the plane of the surface of the nonlinear medium, which appears in the expressions for $\mathbf{k}_I$, $\mathbf{k}$, and $\tilde{\mathbf{k}}$—is a real number and is fixed by boundary conditions for the FEL and NIR fields, which drive the nonlinear polarization, at the interface of the medium with vacuum.

The components of the wave vector $\mathbf{k}$ of the nonlinear polarization wave and its frequency ω are fixed by the frequencies and wave vectors of the fields driving the nonlinear polarization and by the specific nonlinear process, i.e., in our case, third-order sum- and difference-frequency mixing, respectively. Provided that ω_X, $\mathbf{k}_X$ and ω_I, $\mathbf{k}_I$ are the frequencies and wave vectors of the driving FEL and NIR laser fields in the medium, respectively, ω and $\mathbf{k}$ are defined as

$$\omega = \omega_X \pm 2\omega_I$$

$$\mathbf{k} = \mathbf{k}_X \pm 2\mathbf{k}_I$$

This assumes that one FEL photon and two NIR photons are involved in the mixing process as was the case in the experiment.

The amplitude $\mathbf{P}$ of the nonlinear polarization wave in Eq. 2 is set by the third-order nonlinear susceptibility tensor $\chi^{(3)}$ of LiF governing the experimentally studied SFG and DFG. For the cubic LiF crystal structure, only few of the Cartesian components of $\chi^{(3)}$ are different from zero and independent of each other (*36*). In a coordinate system aligned with the crystal axes, a set of independent nonzero components is $\chi^{(3)}_{xxxx}, \chi^{(3)}_{xyyx}, \chi^{(3)}_{xyxy}, \chi^{(3)}_{xxyy}$. We use atomic transition matrix elements among Li^+ states for the purpose of a basic approximation of $\chi^{(3)}$. Therefore, full rotational symmetry prevails for the tensor elements, not just cubic symmetry. This adds an additional constraint to the tensor components, namely, $\chi^{(3)}_{xxxx} = \chi^{(3)}_{xyyx} + \chi^{(3)}_{xyxy} + \chi^{(3)}_{xxyy}$ (*36*). This extended model symmetry and the fact that the LiF dielectric constant is a scalar quantity also mean that the Cartesian coordinate system tied to the experimental plane of incidence in Fig. 2 is equivalent to the coordinate system spanned by the cubic crystal axes. Then, independent of the direction of polarization of the NIR laser beam, the nonlinear polarization component P_y in Eq. 2 is equal to zero, meaning that the field generated is always polarized in the plane of incidence.

The p-type core exciton of LiF at 62.07 eV observed in linear absorption spectra has been attributed to derive from Li^+ dipole allowed transitions from the $(1s)^2$ ground state to excited states (1s2p, $m_l = 0, \pm 1$). A second, much smaller resonance structure on the low-energy side of this p-type resonance has been tentatively associated with a $(1s)^2 - (1s2s)$ Li^+ transition (s-type exciton), not dipole allowed in the free ion (*15*, *17*). A potentially sizable dipole allowed transition matrix element between the (1s2p, $m_l = 0, \pm 1$) and (1s2s) states may, however, influence the third-order nonlinear susceptibility $\chi^{(3)}$ substantially. We thus model $\chi^{(3)}$ of the LiF crystal using just these Li^+ ionic states, ignoring any potential contribution of conduction band states. Our simple model is intended to qualitatively represent the experimentally observed dependence of the reflected sum- and difference-frequency yields on the FEL photon energy (Fig. 3B). Thus, only the ratio of the dipole matrix elements for the Li^+ transitions (1s2s) – (1s2p, $m_l = 0, \pm 1$) and $(1s)^2 - (1s2p, m_l = 0, \pm 1)$ will be relevant for the characterization of $\chi^{(3)}$. Moreover, we will retain the full atomic rotational symmetry for the dipole matrix elements, ignoring crystal field effects. This reduces the number of adjustable parameters in an expression for $\chi^{(3)}$ to the ratio R of the radial parts of these dipole matrix elements. The excitation energies of the p- and s-type core excitons and their widths, assumed to be homogeneous widths, are extracted from the linear reflection data in Fig. 1B. The data used to determine the components of the third-order nonlinear susceptibility are summarized in the Supplementary Materials, and the expression used for our model nonlinear susceptibility is taken from page 93 of (*36*).

A more sophisticated theoretical treatment of the third-order nonlinear susceptibility tensor of LiF in this photon energy range is beyond the scope of this work. It will have to consider a potential influence of conduction band states, account for the excitonic structure more precisely, and take into account the lower cubic crystal symmetry that we replaced by full rotational symmetry in our model. We note that the lower symmetry may have an influence on the relative strengths of the frequency conversion yields, because, in that case, the angle enclosed by the plane of incidence of the laser beams with the LiF crystal axes in the surface plane of the crystal matters (see the Supplementary Materials). Also, we have used a monochromatic approach, whereas the laser pulses have a short pulse duration and possibly a substantial phase modulation accompanied by a corresponding spectral bandwidth that is of the order of the widths of the relevant LiF resonance structures.

SUPPLEMENTARY MATERIALS

Supplementary material for this article is available at https://science.org/doi/10.1126/sciadv.abn5127

REFERENCES AND NOTES

1. H. Danino, I. Freund, Parametric down conversion of x rays into the extreme ultraviolet. *Phys. Rev. Lett.* **46**, 1127–1130 (1981).
2. K. Tamasaku, K. Sawada, E. Nishibori, T. Ishikawa, Visualizing the local optical response to extreme-ultraviolet radiation with a resolution of λ/380. *Nat. Phys.* **7**, 705–708 (2011).
3. A. Schori, C. Bömer, D. Borodin, S. P. Collins, B. Detlefs, M. Moretti Sala, S. Yudovich, S. Shwartz, Parametric down-conversion of x rays into the optical regime. *Phys. Rev. Lett.* **119**, 253902 (2017).
4. T. E. Glover, D. M. Fritz, M. Cammarata, T. K. Allison, S. Coh, J. M. Feldkamp, H. Lemke, D. Zhu, Y. Feng, R. N. Coffee, M. Fuchs, S. Ghimire, J. Chen, S. Shwartz, D. A. Reis, S. E. Harris, J. B. Hastings, X-ray and optical wave mixing. *Nature* **488**, 603–608 (2012).
5. S. Shwartz, M. Fuchs, J. B. Hastings, Y. Inubushi, T. Ishikawa, T. Katayama, D. A. Reis, T. Sato, K. Tono, M. Yabashi, S. Yudovich, S. E. Harris, X-ray second harmonic generation. *Phys. Rev. Lett.* **112**, 163901 (2014).
6. R. K. Lam, S. L. Raj, T. A. Pascal, C. D. Pemmaraju, L. Foglia, A. Simoncig, N. Fabris, P. Miotti, C. J. Hull, A. M. Rizzuto, J. W. Smith, R. Mincigrucci, C. Masciovecchio, A. Gessini, E. Allaria, G. De Ninno, B. Diviacco, E. Roussel, S. Spampinati, G. Penco, S. Di Mitri, M. Trovò, M. Danailov, S. T. Christensen, D. Sokaras, T.-C. Weng, M. Coreno, L. Poletto, W. S. Drisdell, D. Prendergast, L. Giannessi, E. Principi, D. Nordlund, R. J. Saykally, C. P. Schwartz, Soft x-ray second harmonic generation as an interfacial probe. *Phys. Rev. Lett.* **120**, 023901 (2018).
7. F. Bencivenga, R. Cucini, F. Capotondi, A. Battistoni, R. Mincigrucci, E. Giangrisostomi, A. Gessini, M. Manfredda, I. P. Nikolov, E. Pedersoli, E. Principi, C. Svetina, P. Parisse, F. Casolari, M. B. Danailov, M. Kiskinova, C. Masciovecchio, Four-wave mixing experiments with extreme ultraviolet transient gratings. *Nature* **520**, 205–208 (2015).
8. L. Foglia, F. Capotondi, R. Mincigrucci, D. Naumenko, E. Pedersoli, A. Simoncig, G. Kurdi, A. Calvi, M. Manfredda, L. Raimondi, N. Mahne, M. Zangrando, C. Masciovecchio, F. Bencivenga, First evidence of purely extreme-ultraviolet four-wave mixing. *Phys. Rev. Lett.* **120**, 263901 (2018).
9. F. Bencivenga, R. Mincigrucci, F. Capotondi, L. Foglia, D. Naumenko, A. A. Maznev, E. Pedersoli, A. Simoncig, F. Caporaletti, V. Chiloyan, R. Cucini, F. Dallari, R. A. Duncan, T. D. Frazer, G. Gaio, A. Gessini, L. Giannessi, S. Huberman, H. Kapteyn, J. Knobloch,

G. Kurdi, N. Mahne, M. Manfredda, A. Martinelli, M. Murnane, E. Principi, L. Raimondi, S. Spampinati, C. Spezzani, M. Trovò, M. Zangrando, G. Chen, G. Monaco, K. A. Nelson, C. Masciovecchio, Nanoscale transient gratings excited and probed by extreme ultraviolet femtosecond pulses. *Sci. Adv.* **5**, eaaw5805 (2019).
10. E. Shwartz, S. Shwartz, Difference-frequency generation of optical radiation from two-color x-ray pulses. *Opt. Express* **23**, 7471–7480 (2015).
11. C. P. Schwartz, S. L. Raj, S. Jamnuch, C. J. Hull, P. Miotti, R. K. Lam, D. Nordlund, C. B. Uzundal, C. Das Pemmaraju, R. Mincigrucci, L. Foglia, A. Simoncig, M. Coreno, C. Masciovecchio, L. Giannessi, L. Poletto, E. Principi, M. Zuerch, T. A. Pascal, W. S. Drisdell, R. J. Saykally, Angstrom-resolved interfacial structure in buried organic-inorganic junctions. *Phys. Rev. Lett.* **127**, 096801 (2021).
12. J. R. Rouxel, D. Fainozzi, R. Mankowsky, B. Rösner, G. Seniutinas, R. Mincigrucci, S. Catalini, L. Foglia, R. Cucini, F. Döring, A. Kubec, F. Koch, F. Bencivenga, A. A. Haddad, A. Gessini, A. A. Maznev, C. Cirelli, S. Gerber, B. Pedrini, G. F. Mancini, E. Razzoli, M. Burian, H. Ueda, G. Pamfilidis, E. Ferrari, Y. Deng, A. Mozzanica, P. J. M. Johnson, D. Ozerov, M. G. Izzo, C. Bottari, C. Arrell, E. J. Divall, S. Zerdane, M. Sander, G. Knopp, P. Beaud, H. T. Lemke, C. J. Milne, C. David, R. Torre, M. Chergui, K. A. Nelson, C. Masciovecchio, U. Staub, L. Patthey, C. Svetina, Hard x-ray transient grating spectroscopy on bismuth germanate. *Nat. Photonics* **15**, 499–503 (2021).
13. J. D. Gaynor, A. P. Fidler, Y.-C. Lin, H.-T. Chang, M. Zuerch, D. M. Neumark, S. R. Leone, Solid state core-exciton dynamics in NaCl observed by tabletop attosecond four-wave mixing spectroscopy. *Phys. Rev. B* **103**, 245140 (2021).
14. R. Haensel, C. Kunz, B. Sonntag, Measurement of photoabsorption of the lithium halides near the lithium *K* edge. *Phys. Rev. Lett.* **20**, 262–264 (1968).
15. W. Olovsson, I. Tanaka, P. Puschnig, C. Ambrosch-Draxl, Near-edge structures from first principles all-electron Bethe-Salpeter equation calculations. *J. Phys. Condens. Matter* **21**, 104205 (2009).
16. S. T. Pantelides, Electronic excitation energies and the soft-x-ray absorption spectra of alkali halides. *Phys. Rev. B* **11**, 2391–2411 (1975).
17. J. R. Fields, P. C. Gibbons, S. E. Schnatterly, Electronic excitations in LiF: 10-70 eV. *Phys. Rev. Lett.* **38**, 430–434 (1977).
18. E. L. Shirley, Li 1s near-edge spectra in six lithium halides. *J. Electron Spectros. Relat. Phenomena* **137-140**, 579–584 (2004).
19. W. Olovsson, I. Tanaka, T. Mizoguchi, P. Puschnig, C. Ambrosch-Draxl, All-electron Bethe-Salpeter calculations for shallow-core x-ray absorption near-edge structures. *Phys. Rev. B* **79**, 041102 (2009).
20. A. B. Kunz, J. C. Boisvert, T. O. Woodruff, Li *K*-edge soft-x-ray absorption in LiF. *Phys. Rev. B* **30**, 2158–2162 (1984).
21. A. B. Kunz, J. T. Devreese, T. Collins, The role of the electronic polaron in the soft X-ray absorption of the lithium halides. *J. Phys. C Solid State Phys.* **5**, 3259–3263 (1972).
22. B. F. Sonntag, Observations of "forbidden" soft-x-ray transitions: Li *K* absorption in LiF. *Phys. Rev. B* **9**, 3601–3602 (1974).
23. W. Gudat, C. Kunz, H. Petersen, Core exciton and band structure in LiF. *Phys. Rev. Lett.* **32**, 1370–1373 (1974).
24. T. Sato, R. Letrun, H. J. Kirkwood, J. Liu, P. Vagovič, G. Mills, Y. Kim, C. M. S. Takem, M. Planas, M. Emons, T. Jezynski, G. Palmer, M. Lederer, S. Schulz, J. Mueller, H. Schlarb, A. Silenzi, G. Giovanetti, A. Parenti, M. Bergemann, T. Michelat, J. Szuba, J. Grünert, H. N. Chapman, A. P. Mancuso, Femtosecond timing synchronization at megahertz repetition rates for an X-ray free-electron laser. *Optica* **7**, 716 (2020).
25. S. Schulz, I. Grguraš, C. Behrens, H. Bromberger, J. T. Costello, M. K. Czwalinna, M. Felber, M. C. Hoffmann, M. Ilchen, H. Y. Liu, T. Mazza, M. Meyer, S. Pfeiffer, P. Prędki, S. Schefer, C. Schmidt, U. Wegner, H. Schlarb, A. L. Cavalieri, Femtosecond all-optical synchronization of an X-ray free-electron laser. *Nat. Commun.* **6**, 5938 (2015).
26. J. Duris, S. Li, T. Driver, E. G. Champenois, J. P. MacArthur, A. A. Lutman, Z. Zhang, P. Rosenberger, J. W. Aldrich, R. Coffee, G. Coslovich, F.-J. Decker, J. M. Glownia, G. Hartmann, W. Helml, A. Kamalov, J. Knurr, J. Krzywinski, M.-F. Lin, J. P. Marangos, M. Nantel, A. Natan, J. T. O'Neal, N. Shivaram, P. Walter, A. L. Wang, J. J. Welch, T. J. A. Wolf, J. Z. Xu, M. F. Kling, P. H. Bucksbaum, A. Zholents, Z. Huang, J. P. Cryan, A. Marinelli, Tunable isolated attosecond X-ray pulses with gigawatt peak power from a free-electron laser. *Nat. Photonics* **14**, 30–36 (2020).
27. A. A. Maznev, R. Mincigrucci, F. Bencivenga, V. Unikandanunni, F. Capotondi, G. Chen, Z. Ding, R. A. Duncan, L. Foglia, M. G. Izzo, C. Masciovecchio, A. Martinelli, G. Monaco, E. Pedersoli, S. Bonetti, K. A. Nelson, Generation and detection of 50 GHz surface acoustic waves by extreme ultraviolet pulses. *Appl. Phys. Lett.* **119**, 044102 (2021).
28. E. Berger, S. Jamnuch, C. B. Uzundal, C. Woodahl, H. Padmanabhan, A. Amado, P. Manset, Y. Hirata, Y. Kubota, S. Owada, K. Tono, M. Yabashi, C. Wang, Y. Shi, V. Gopalan, C. P. Schwartz, W. S. Drisdell, I. Matsuda, J. W. Freeland, T. A. Pascal, M. Zuerch, Extreme ultraviolet second harmonic generation spectroscopy in a polar metal. *Nano Lett.* **21**, 6095–6101 (2021).
29. D. Popova-Gorelova, D. A. Reis, R. Santra, Theory of X-ray scattering from laser-driven electronic systems. *Phys. Rev. B* **98**, 224302 (2018).
30. R. Cohen, S. Shwartz, Theory of nonlinear interactions between x rays and optical radiation in crystals. *Phys. Rev. Res.* **1**, 033133 (2019).
31. J. R. Rouxel, M. Kowalewski, K. Bennett, S. Mukamel, X-ray sum frequency diffraction for direct imaging of ultrafast electron dynamics. *Phys. Rev. Lett.* **120**, 243902 (2018).
32. M. Beye, R. Y. Engel, J. O. Schunck, S. Dziarzhytski, G. Brenner, P. S. Miedema, Non-linear soft x-ray methods on solids with MUSIX–the multi-dimensional spectroscopy and inelastic X-ray scattering endstation. *J. Phys. Condens. Matter* **31**, 014003 (2019).
33. L. Raimondi, C. Svetina, N. Mahne, D. Cocco, A. Abrami, M. De Marco, C. Fava, S. Gerusina, R. Gobessi, F. Capotondi, E. Pedersoli, M. Kiskinova, G. De Ninno, P. Zeitoun, G. Dovillaire, G. Lambert, W. Boutu, H. Merdji, A. Gonzalez, D. Gauthier, M. Zangrando, Microfocusing of the FERMI@Elettra FEL beam with a K–B active optics system: Spot size predictions by application of the WISE code. *Nucl. Instrum. Methods Phys. Res. Sect. A Accel. Spectrometers Detect. Assoc. Equip.* **710**, 131–138 (2013).
34. A. A. Sorokin, Y. Bican, S. Bonfigt, M. Brachmanski, M. Braune, U. F. Jastrow, A. Gottwald, H. Kaser, M. Richter, K. Tiedtke, An X-ray gas monitor for free-electron lasers. *J. Synchrotron Radiat.* **26**, 1092–1100 (2019).
35. T. Kachel, The PM3 beamline at BESSY II. *J. large-scale Res. Facil. JLSRF* **2**, A48 (2016).
36. P. N. Butcher, D. Cotter, *The Elements of Nonlinear Optics* (Cambridge Univ. Press, 1990).
37. A. Milgram, M. P. Givens, Extreme ultraviolet absorption by lithium fluoride. *Phys. Rev.* **125**, 1506–1509 (1962).
38. J. D. Jackson, *Classical Electrodynamics* (John Wiley & Sons Inc., ed. 3, 1998).
39. M. Braune, J. Buck, M. Kuhlmann, S. Grunewald, S. Düsterer, J. Viefhaus, K. Tiedtke, Non-invasive online wavelength measurements at FLASH2 and present benchmark. *J. Synchrotron Radiat.* **25**, 3–15 (2018).
40. B. L. Henke, E. M. Gullikson, J. C. Davis, *X-Ray Interactions With Matter* (U.S. Department of Energy, 1993).
41. B. Henke, E. Gullikson, J. Davis, X-ray interactions: Photoabsorption, scattering, transmission, and reflection at E = 50-30,000 eV, Z = 1-92. *At. Data Nucl. Data Tables* **54**, 181–342 (1993).

Acknowledgments: We acknowledge DESY (Hamburg, Germany), a member of the Helmholtz Association HGF, for the provision of experimental facilities. Parts of this research were carried out at FLASH, beamline FL24, using the MUSIX end station. Beamtime was allocated for proposal F-20181181. Other parts of the research were carried out at the PM3 beamline at the BESSY II electron storage ring operated by the Helmholtz-Zentrum Berlin für Materialien und Energie. **Funding:** This work was supported by Helmholtz foundation grant VH-NG-1105 (to R.Y.E, J.O.S., P.S.M., and M.B.) **Author contributions:** Conceptualization: H.R., S.E., and M.B. Experiment: H.R., R.Y.E., J.O.S., P.S.M., M.C.B., M.K., N.E., S.D., G.B., U.E., D.S., and C.v.K.S. Data analysis: R.Y.E. and H.R. Theoretical model and calculations: H.R. Visualization: H.R., R.Y.E, and D.S. Interpretation: H.R., S.E., R.Y.E., and M.B. Writing—original draft: H.R., D.S., and S.E. (with input from all authors). Writing—revision and reply: H.R., R.Y.E., D.S., and S.E. **Competing interests:** The authors declare that they have no competing interests. **Data and materials availability:** All data needed to evaluate the conclusions in the paper are present in the paper and/or the Supplementary Materials. In addition, we provide the presented data within the following repository: 10.5281/zenodo.5723994.

Submitted 13 December 2021
Accepted 5 April 2022
Published 20 May 2022
10.1126/sciadv.abn5127